# Milling effect on the photo-activated properties of $TiO\_2$ nanoparticles: electronic and structural investigations

Youcef Messai, Bertrand Vileno, David Martel, Philippe Turek, Djamel Eddine Mekki

*Bull. Mater. Sci.* (2018) 41:57
https://doi.org/10.1007/s12034-018-1572-8



# Milling effect on the photo-activated properties of $TiO_2$ nanoparticles: electronic and structural investigations

**YOUCEF MESSAI[1,2], BERTRAND VILENO[2,4], DAVID MARTEL[3], PHILIPPE TUREK[2,4] and DJAMEL EDDINE MEKKI[1,*]**

[1]Laboratoire d'Etude des Surfaces et Interfaces de la Matière Solide (LESIMS), Université Badji Mokhtar, 23000 Annaba, Algeria

[2]Institut de Chimie (UMR 7177, CNRS-Unistra), Université de Strasbourg, 1 rue Blaise Pascal, CS 90032, 67081 Strasbourg Cedex, France

[3]CNRS, Institut Charles Sadron, Université de Strasbourg, 23 rue du Lœss, 67000 Strasbourg, France

[4]French EPR Federation of Research (REseau NAtional de RPEinterDisciplinaire (RENARD), Fédération IR-RPE CNRS #3443), Strasbourg, France

*Author for correspondence (mekki.djameleddine57@gmail.com)

MS received 12 July 2017; accepted 21 August 2017; published online 30 March 2018

**Abstract.** Commercial PC105 titanium dioxide nanoparticles were studied under mechanical milling process. The effect of milling time and speed on the structural and electronic properties of $TiO_2$ powder was then investigated using X-ray powder diffraction (XRD), dynamic light scattering (DLS), transmission electronic microscopy (TEM), electron paramagnetic resonance (EPR) and UV–visible spectroscopy. The related photo-catalytic properties of the milled nanoparticles were probed following the degradation rate of methylene orange (MO) under UV-light irradiation and through EPR spin-scavenging approach. Comparison with pristine powder shows that milled nanoparticles are significantly less reactive upon illumination, despite decreased radius and hence, higher specific area. Such low yield of reactive species is attributed to the apparition of the amorphous $TiO_2$ and brookite phase upon milling, as well as increased charge carrier recombination as pointed out by the presence of sacrificial electron donor.

**Keywords.** Titania nanoparticles; ball milling; photo-catalytic properties; photo-generated radicals; electronic paramagnetic resonance spectroscopy.

## 1. Introduction

Nowadays, nanoparticles (NPs) find numerous and increasing uses in many fields of technology. This trend is foreseen to considerably expand in the near future, ranging from biology to medicine, energy storage, environment, pigment or cosmetic industries [1–3]. This wide variety of applications is undoubtedly related to their peculiar characteristics that include particle shape, specific area, charge, chemistry, dispersion and/or agglomeration characteristics, aggregate size and shape distribution, solubility and porosity [4–7].

Remarkably, the research towards the development of highly active heterogeneous photo-catalysts, naturally oriented towards transition metal oxides (TMOs, such as $TiO_2$, ZnO, $SnO_2$) that are semiconductors (SC) with a gap allowing good absorption of light in the UV and/or in the near-visible range. These SC-based NPs often exhibit improved photo-catalytic properties due to enhanced surface/volume ratio. When combined with the so-called methods of advanced oxidation processes (AOP) [8], these materials are known to be efficient decontaminant:neutralizing bacteria and viruses [9,10], as well as degrading organic pollutants within air and water [11]. Such high applicative potential involves various processes ranging from photolysis via $H_2O_2$ [12], to Fenton or photo-Fenton effect [13], where photo-mediated reactive oxygen species (ROS) are playing central role.

Among TMOs, $TiO_2$ is considered as one of the most promising for wide environmental- and energy-applications, because of its suitable valence and conduction band positions, long-term stability, cost-effectiveness and strong oxidizing power [14]. It is a polymorphic material with three main distinct phases [15]: anatase (tetragonal phase, $I4_1/amd$ space group, indirect band gap, $E_g = 3.2$ eV), rutile (stable tetragonal phase, $P4_2/mnm$ space group, direct band gap, $E_g = 3.0$ eV) and brookite (stable orthorhombic phase, Pbca space group, direct band gap $E_g = 3.3$ eV) [16,17].

*Electronic supplementary material: The online version of this article (https://doi.org/10.1007/s12034-018-1572-8) contains supplementary material, which is available to authorized users.*

While with a higher surface adsorption capacity to hydroxyl groups, anatase was shown to present lower charge carrier recombination rate than rutile [18,19]. Indeed, the lifetime of photo-generated electrons and holes in anatase is about an order of magnitude greater than one of the rutile. This greatly promotes their contribution to surface chemical reactions [20]. Moreover, the average effective mass of photo-generated electrons and holes in anatase displays smaller value in comparison to rutile and brookite [21]. The transfer rate of photo-generated electrons and holes being inversely proportional to their effective masses [17], the photo-excited charge carriers of anatase is thus transferred faster to the semiconductor surface [22]. These facts bear out the idea that $TiO_2$ in its anatase form shows better photo-catalytic performance than rutile and brookite [12,23,24]. Regarding the present study, it was shown that ROS are photo-generated via $TiO_2$ NPs suspension under UV illumination [25,26].

There are several methods to prepare $TiO_2$ NPs, such as sol–gel [27], micro emulsion [28], hydro- and solvo-thermal [29] precipitations or co-precipitations [30,31]. Mechanical milling (MM) is also widely used, as it is a cheap, efficient and relatively simple technique to handle. During the process, powder particles are subjected to severe mechanical deformations and are repeatedly deformed, heat-treated (cooling and warming), welded and fractured, inducing their gradual refinement to nanometer scale [22,32–34]. Consequently, unusual properties could appear via the emergence of structural defects that can be charged or not.

Although numerous articles report on the correlation between photo-catalytic activity and the physical properties [35,36] (particle size [37], crystal structure [38,39], surface area [40]), recent investigations challenged such conclusions [41,42]. Among the available experimental approaches, MM at high energy is an established method to modify physical properties [43], aiming to improve the material properties. Nevertheless, the consequences of milling on $TiO_2$ NPs are still debated. Rezae *et al* [44] showed that MM for 6 h causes a complete conversion of the anatase phase to the brookite and rutile phases. Other recent studies indicate that milling of $TiO_2$ NPs results in an amorphous material [45,46], which is photo-catalytically inactive [47]. Moreover, Bégin *et al* [45] observed the degradation of the photo-catalytic properties of $TiO_2$ NPs after MM and attributed it to new channels of radiative recombination produced upon milling. Indeed, partial amorphization of NP surfaces induces an increase of surface defect density and offers electron/hole ($e^-/h^+$) recombination pathways. The $e^-/h^+$ recombination rate in presence of amorphous phase occurs more quickly when compared to any pure crystalline phase [36]. Such conclusions were also achieved in very recent work by Aggelopoulos *et al* [48], comparing ZnO and $TiO_2$ NPs. Nevertheless, Saitow and Wakamiya [46] showed an impressive 130-fold enhancement of the photo-catalytic properties of NPs $TiO_2$ prepared by planetary ball milling, pointing to the controversy of scientific debate. Such enhancement was attributed by the authors to the disordered, amorphous state together with the srilankite phase of $TiO_2$ NPs produced upon milling.

The present work deals with the effects of MM conditions (time and speed) on anatase $TiO_2$ NPs through the resulting structural modifications and electronic properties as well as the photo-catalytic activity towards MO degradation. The structural and morphological properties of the studied NPs were investigated by classical X-ray diffraction (XRD), transmission electron microscopy (TEM) and dynamic light scattering (DLS). The electronic properties were analysed by means of UV–visible spectroscopy of the solid state. Additionally, electronic paramagnetic resonance (EPR) spectroscopy was performed to probe the photo-mediated reactive species by using spin-scavenging approach via 4-hydroxy-2,2,6,6-tetramethylpiperidin-1-oxyl (TEMPOL) reduction [49]. All the obtained results are compared with the properties of pristine $TiO_2$ nanoparticles.

## 2. Materials and methods

### 2.1 *MM*

Anatase $TiO_2$ (PC105) NPs were purchased from Crystal Global. Average NP size is of *ca.* 25 nm, surface area estimated at *ca.* 90 $m^2\ g^{-1}$ and the weight purity is of *ca*. 95%. Samples of PC105 (1.7 g) with a ratio of 97:3 from ball masses *vs*. NP powders was charged under an Ar atmosphere in high-energy planetary ball mill (FRISCH premium line). Milled NPs were successfully obtained with two speed conditions ($\Omega = 200$ and 400 rpm) and four different milling times ($t = 1,\ 3,\ 5$ and 7 h) for each speed.

### 2.2 *XRD*

$TiO_2$ NPs XRD spectra were carried out with a panalytical Phillips X'Pert Pro diffractometer, equipped with a $CuK\alpha_1$ anticathode ($\lambda = 0.15406$ nm). The XRD patterns were recorded between 20 and 90° with a monitoring step of 0.03°.

### 2.3 *DLS*

A Zetasizer Nano ZS (Malvern, $\lambda = 633$ nm) and a disposable folded capillary cell were used to measure the hydrodynamic diameter of the aggregated $TiO_2$ NPs in aqueous suspension. All the hydrodynamic diameter distributions correspond to number distributions.

### 2.4 *TEM*

The morphology and crystalline structure of $TiO_2$ NPs were studied with a Tecnai G2 20 Twin TEM. An aqueous suspension of $TiO_2$ (0.1 $g\ l^{-1}$) was sonicated for 15 min to reduce the granulation. Five microlitres of this suspension was deposited onto a grid covered by a thin carbon film.

### 2.5 *Optical characterization*

Band gaps were determined via optical measurements. UV–visible spectra of $TiO_2$ powders were recorded at room temperature in reflection mode in the range of 200–800 nm with a JASCO V-750 spectrometer, equipped with an integrating sphere model #ILN-725.

### 2.6 *Photo-catalytic activity*

2.6a *MO degradation*: Aqueous suspensions (250 ml) of $TiO_2$ NPs (200 mg $l^{-1}$) and 45 μM of MO (purchased from Aldrich) were prepared. Prior to any illumination step, the suspensions were stirred in the dark for 30 min. The suspensions were subsequently irradiated with a UV lamp (Vilber Lourmat VL-215-BL, $\lambda_{max} = 365$ nm, $P = 60$ W) located at 15 cm from the sample to avoid heating of the suspension and pigment bleaching. The suspensions were stirred during the whole experiment and the temperature was kept at 298 ± 2K. Two and a half millilitres of the working solution was repeatedly withdrawn from the working suspension, centrifuged and the supernatant was analysed by UV–visible spectroscopy performed in transmission mode with a JASCO V-750 spectrometer. The present experimental data show the decay of the absorbance recorded at the wavelength of $\lambda = 480$ nm (see supplementary figure S1b) and normalized to the value obtained prior to the first illumination. The adsorption of the MO onto the NPs surfaces was found to be negligible (<5% of the dye concentration after 3 h in contact with the $TiO_2$ suspension), the threshold being reached after 30 min (data not shown).

2.6b *EPR spin-scavenging*: Experimental protocol was derived from the existing methodology described elsewhere [50,51]. Continuous-wave (cw) EPR spectra were recorded at room temperature using an X-band ECS 106 (Bruker-Biospin GmbH, Germany) spectrometer equipped with a regular TE102 resonator. This setup was used to record the conventional field-swept spectra from the aqueous suspensions containing $TiO_2$ suspensions (0.1 g $l^{-1}$) and 200 μM of TEMPOL (purchased from Aldrich) in ultrapure water (18.2 MΩ $cm^{-1}$). TEMPOL is a paramagnetic probe (i.e., active) known to react with small-sized radicals leading to diamagnetic and hence, EPR silent byproducts [50]. Therefore, its decay is testimony of the photo-mediated generation of reactive species. The EPR spectrum of 200 μM prior illumination is presented in supplementary figure S1a. Ethylenediamine tetraacetic acid (EDTA, purchased from Aldrich) was also used in this work as electron sacrificial donor. Prior to measurements, the solutions (1 ml) were sonicated (15 min in a sonicator bath). Afterwards, the solutions were immediately transferred into thin-wall glass capillaries (Hirschmannrin caps, 50 μl), which were sealed at both ends. Illumination of the sealed capillaries was performed outside the cavity with a UV light source Vilber Lourmat T-4.L ($\lambda_{max} = 365$ nm and $E(1\text{ cm}) \approx 1.5$ mW $cm^{-2}$ measured with a power meter 1936-C Newport). The EPR spectra were recorded after each irradiation step. The main experimental parameters were: microwave power of 2 mW, time constant of 40 ms, conversion time of 80 ms and sweeping of 100G leading to *ca.* 80 s of accumulation per scan. All experiments were performed at room temperature (295 ± 2K).

### 2.7 *EPR measurements at low temperature*

Sixty milligrams of $TiO_2$ powder were introduced in a 4 mm outer diameter quartz tube and degassed for *ca.* 10 min at room temperature. The cw-EPR spectra were recorded at 25K with a micro X-EMX spectrometer (BrukerBiospin GmbH, Germany) equipped with a high sensitivity resonator (4119HS-W1, BrukerBiospin GmbH, Germany) and liquid He cryostat (ESR900, Oxford Instrument).

## 3. Results and discussion

### 3.1 *Structural properties*

XRD patterns of $TiO_2$ NPs are shown in figure 1a and b for the two values of milling speed ($\Omega = 200$ and 400 rpm, respectively), different milling times (1–7 h) and the reference sample ($t = 0$ h).

Several diffraction peaks are observed for $\Omega = 200$ rpm (figure 1a) at the following angular positions: $2\theta = 25$, 37.8, 48.5, 53.95, 55, 62.6, 68.9, 70.1, 75 and 82°. These peaks were identified according to the JCPDS card (21-1272) as the (101), (112), (200), (105), (211), (204), (116), (220), (215) and (303) Bragg's planes of the anatase $TiO_2$ structure. The relative ratios between peaks, for a given sample, are almost constant. Furthermore, new peaks were detected for the two longer milling times ($t = 5$ and 7 h), where the small bump detected around $2\theta = 30.8°$ can be testimony of brookite phase [41]. Clearly, the more the NPs were milled, the more the data appeared noisy and present a significant baseline at small angles, indicating the rising of an amorphous state.

In contrast, for the high energy milling at $\Omega = 400$ rpm (figure 1b), the peak intensities decrease rapidly. After 1 h milling, the similar amorphous finger print is rising together with a peak close to $2\theta = 30.8°$, pointing to brookite phase.

### 3.2 *NPs characterization*

Average of the grain sizes $D$ of NPs $TiO_2$ were estimated with Scherrer formula, equation (1) [52,53].

$$D = \frac{K\lambda}{\beta \cos\theta}, \tag{1}$$

where $K = 0.94$, $\theta$ is the angle of diffraction, $\lambda$ the X-ray wavelength, $\beta$ the full-width at half-height of a peak corresponding to a given orientation.

The grain sizes were also assessed from TEM observation and are summarized in table 1. The curves resulting from

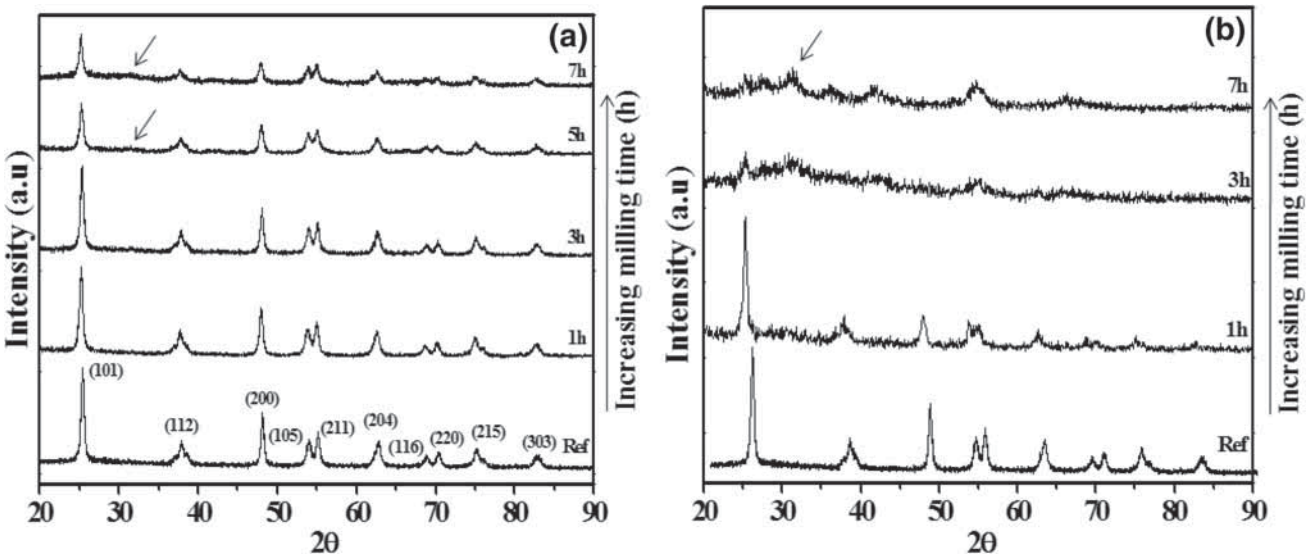


**Figure 1.** XRD patterns of NPs $TiO_2$ before milling and at various milling times for the milling speed (**a**) 200 and (**b**) 400 rpm.

**Table 1.** Grain sizes as a function of milling time for the speeds $\Omega = 200$ and 400 rpm.

| Milling time (h) | 0 | 1 | 3 | 5 | 7 |
|---|---|---|---|---|---|
| Grain size (nm) DRX (200 rpm) | 23 | 18 | 13 | 13 | 13 |
| Grain size (nm) $\pm$ $\sigma$ via TEM (200 rpm) | $19.9 \pm 6.9$ | $14.9 \pm 5.1$ | $11.9 \pm 3.9$ | $12.8 \pm 5.2$ | $13.4 \pm 4.4$ |
| Grain size (nm) DRX (400 rpm) | 23 | 19 | — | — | — |
| Grain size (nm) $\pm$ $\sigma$ via TEM (400 rpm) | $19.9 \pm 6.4$ | $15.4 \pm 6.2$ | $10.5 \pm 3.6$ | — | $9.8 \pm 2.9$ |

TEM data analysis and representing the grain size distribution (fitted with Gaussian functions) for all the samples milled at $\Omega = 200$ and 400 rpm are given in supplementary figure S2. Accordingly, the grain size varies between 5 and 45 nm. Whatever the XRD or TEM data, grain size significantly decreases from *ca.* 20 to 12 nm after 3 h of milling at the lowest speed. At the highest speed, a similar trend is observed with a decrease from *ca.* 20 to 10 nm. The average size of the grain deduced from TEM observations is in good agreement with the one calculated from XRD using Scherrer formula (table 1).

Figure 2 shows the TEM micrographs of $TiO_2$ NPs for various conditions of milling times ($t$ = reference, 1, 3, 5 and 7 h) and speeds ($\Omega = 200$ and 400 rpm). During MM, the NPs are subjected to severe mechanical deformations, leading to a progressive evolution of their shape and mean grain size. However, it seems that experiments at higher grinding times would have produced more uniform size distribution and homogeneous spherical shapes. This trend is expected when the high energy ball milling process reach a steady state, where a balance happens between cold welding and fracturing operations [54]. It is to be noticed that these effects are sharper at higher speed (see figure 2).

It is also known that one of the possible consequences of the MM process is the appearance of amorphous and/or unstable phases [55]. It was therefore, interesting to appreciate and observe these phases. For this purpose, TEM images were interpreted by means of a fast Fourier transform (FFT) for milling speed condition, $\Omega = 200$ rpm. Figure 3 shows the FFT of an amorphous grain (single spot) and well-defined crystalline grains (spots distributed with respect to the crystal symmetry). Two lattice spacings of 0.35 and 0.9 nm are measured, which are assigned to the (101) of anatase and (100) plane of the brookite phase [56], respectively, revealed after 3 h milling [57].

## 4. DLS analysis

It is known that the transition metal oxides aggregate considerably in aqueous solution [58,59]. As the yield of reactive species is influenced by the available surface and the surface states, the knowledge of the characteristics of the aggregation state is required. For this purpose, both milled and reference samples were characterized by DLS to estimate the hydrodynamic diameter of aggregated NPs. All data were fitted with a Gaussian function and for clarity purpose, only the resulting fits are represented in figure 4.

The materials before milling ($t = 0$) in suspension have an average diameter of *ca.* 1 μm (figure 4). Notably, this size remains constant (*ca.* 550 nm) for all milled $TiO_2$ NPs

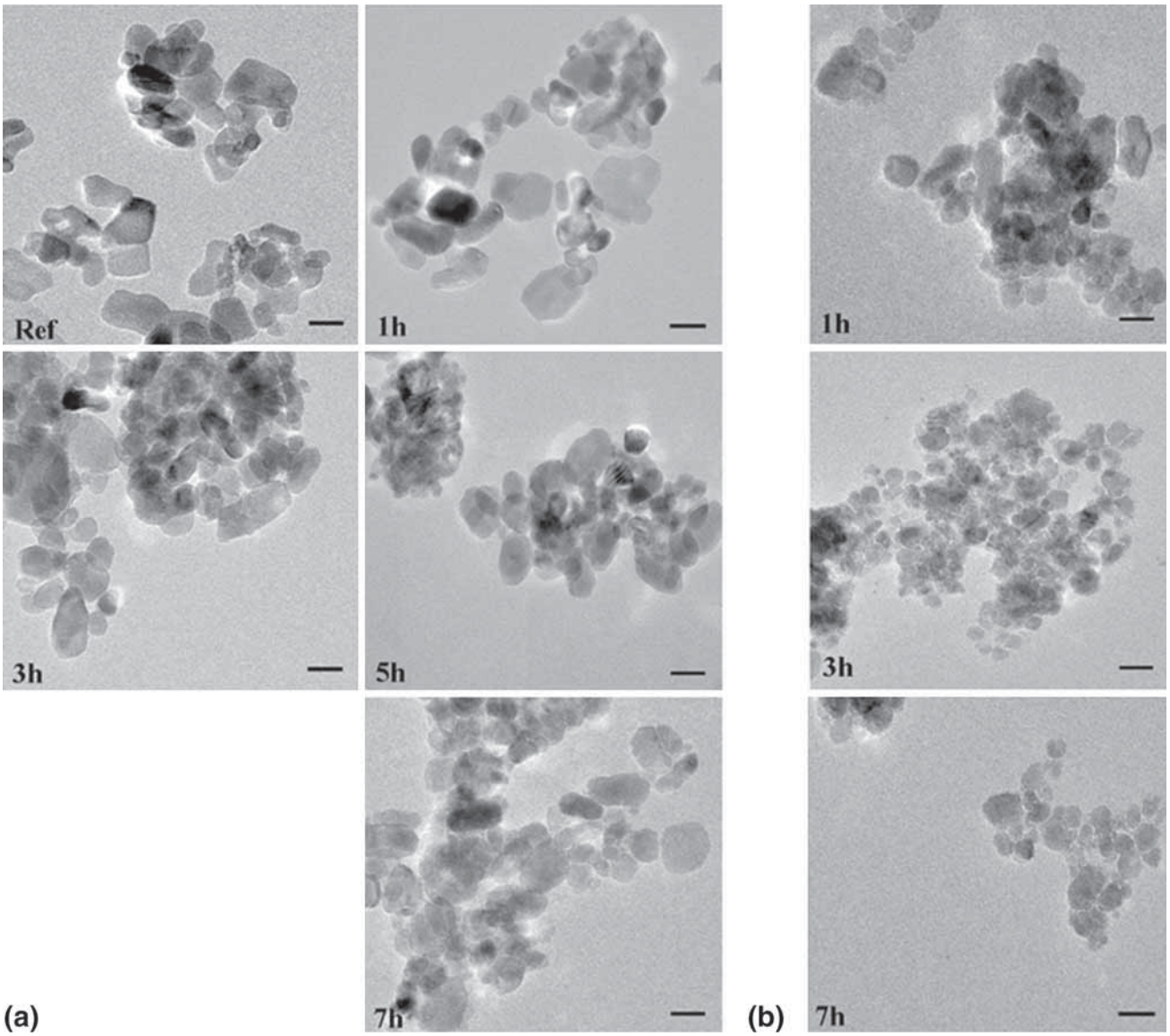


**Figure 2.** TEM images showing the morphology of $TiO_2$ NPs before and after milling $t = 0$ (reference), 1, 3, 5 and 7 h with speed $\Omega =$ (**a**) 200 and (**b**) 400 rpm. Scale bar corresponds to 20 nm.

at $\Omega = 200$ rpm. Surprisingly, the hydrodynamic diameter of sample milled at $\Omega = 400$ rpm dropped down to *ca.* 200 nm after 1 h milling time, but reproducibly returns to *ca.* 1 μm; i.e., similar to 3 and 7 h milling times as well as reference sample (figure 4b). Moreover, although the particle sizes obtained for both milling speeds and equivalent milling times are similar (see table 1), the subsequent hydrodynamic diameter do not present the same similarities. This suggests a considerable influence of the milling condition on the nature of the NPs surface states that drive the aggregation phenomenon.

### 4.1 *Optical properties and electronic structure*

Figure 5 displays the diffuse reflectance properties, for commercial (reference sample) and milled $TiO_2$ NPs at all rotation speeds and milling times. Typical fingerprint of $TiO_2$ NPs crystallite in the UV range is obtained.

However, the milling process induced a slight shift of the absorption edge towards higher wavelength, regardless of the speed. Consequently, as MM generates different type of defects (such as surface, lattice strain, vacancy, interstitial, dislocation, grain boundary, etc.), additional states appear within the band gap of $TiO_2$, create band tails extending of the valence and conduction band edges [60]. Two important parameters are naturally impacted by this physical situation, namely the optical gap ($E_g$) and the Urbach energy ($E_u$) pointing to changes in the electronic structure (doping, disorder, etc.). To assess $E_g$ and $E_u$, the absorption coefficients $F(R)$ are deduced from the reflectance curves, according to

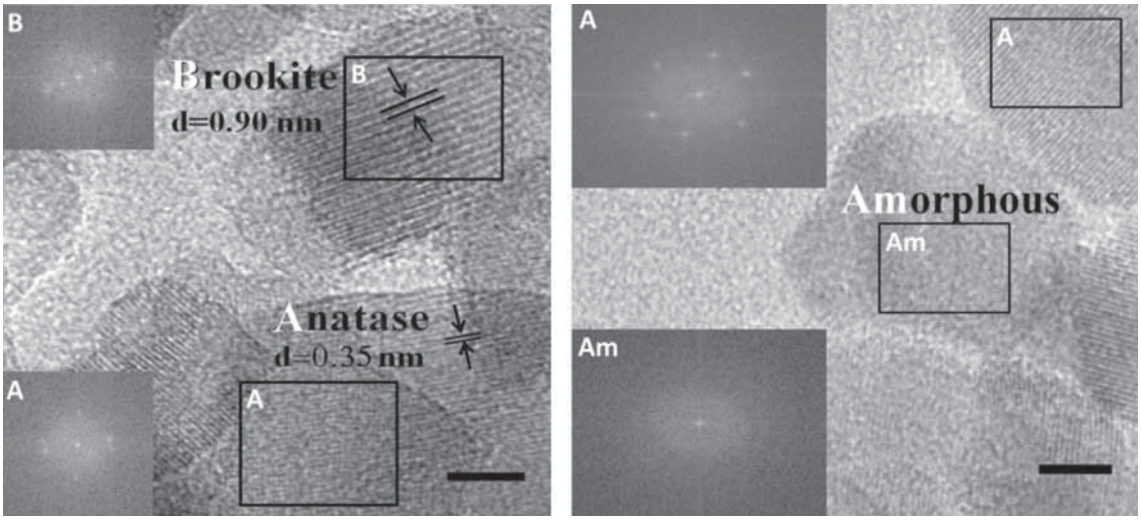


**Figure 3.** High-resolution TEM images of NPs $TiO_2$ (after 3 h of milling at $\Omega = 200$ rpm) showing the crystalline anatase (A), brookite (B) and amorphous (Am) phases. The insets correspond to the local FFT and the scale bars correspond to 5 nm.

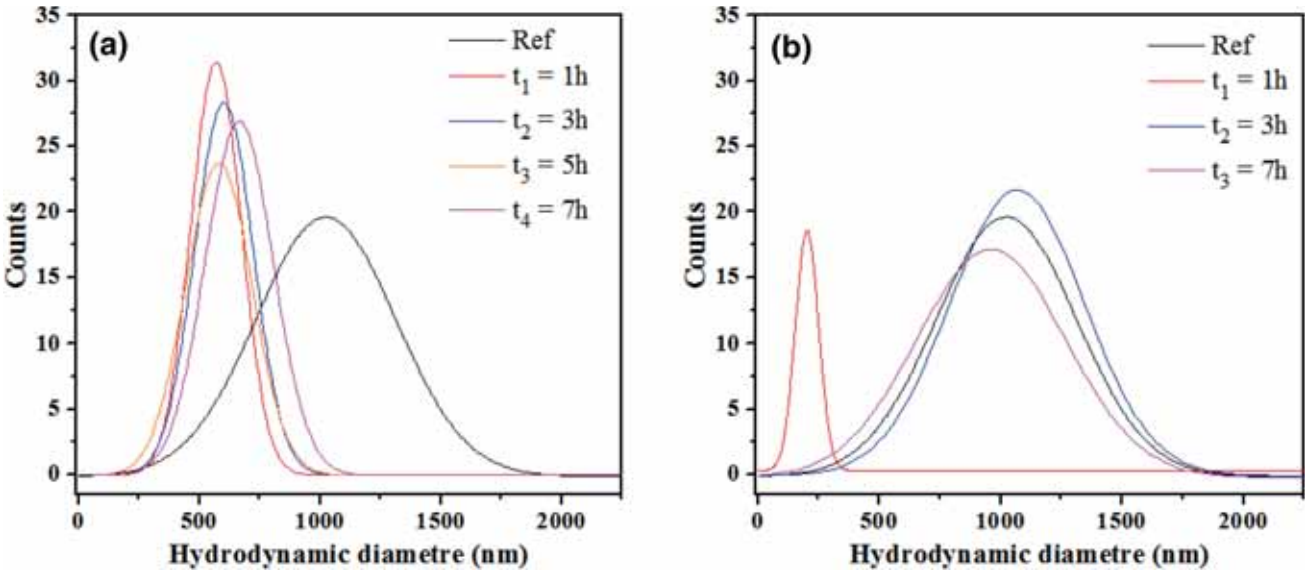


**Figure 4.** Distribution of the hydrodynamic diameter in an aqueous suspension of milled compounds and reference sample (0.1 g $l^{-1}$), with $\Omega =$ (**a**) 200 and (**b**) 400 rpm.

the Kubelka–Munk equation [61–63]:

$$F(R) = \frac{(1-R)^2}{2R}, \tag{2}$$

where $R$ is the reflectance, and $F(R)$ is equivalent to the absorption coefficient ($\alpha$). The band gap, $E_g$ is evaluated through the Tauc plot on the linear part of $(\alpha h\nu)^n \propto h\nu - E_g$ (where $n = 1/2$ for indirect band gap) for $(\alpha h\nu)^{1/2} = 0$ (see figure 6).

The Urbach energy, $E_u$ is given by the following phenomenological relation [64], where $\alpha_0$ and $E_0$ are constants related to the studied material:

$$\alpha = \alpha_0 \exp\frac{h\nu - E_0}{E_u}. \tag{3}$$

Figure 7a and b represent the respective variations of $E_g$ and $E_u$ as a function of milling time for both the values of $\Omega$. It is observed that as expected, $E_g$ and $E_u$ have opposite evolution curves. Nevertheless, the more the value of $\Omega$ is high, the more its influence is obvious for $E_g$, rather than for $E_u$. Finally, the influence of grain size on the variations of the Urbach energy, $E_u$ and the optical band gap, $E_g$ is highlighted in figure 7c

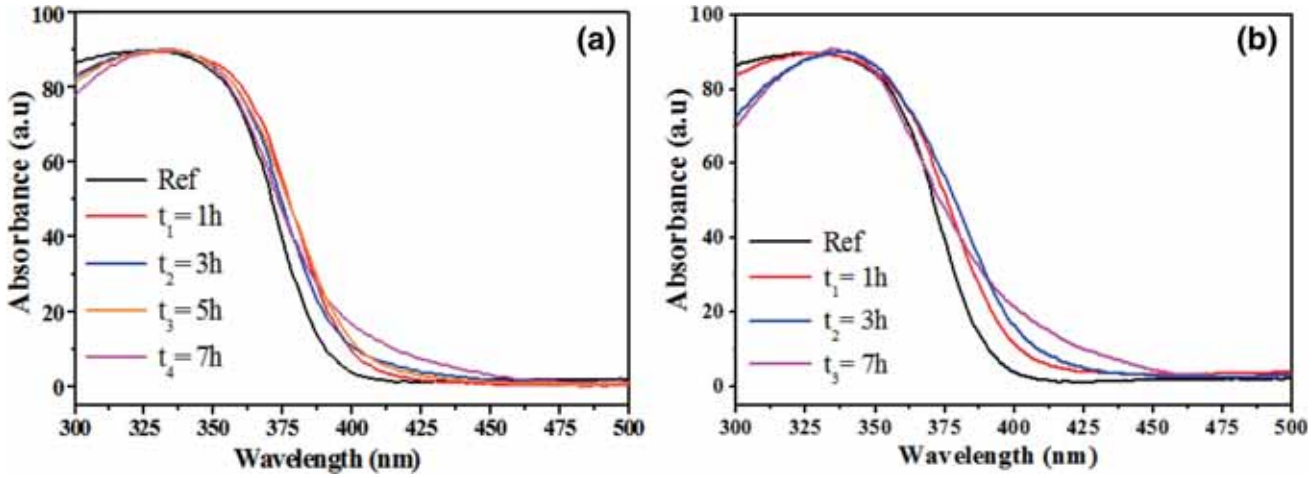


**Figure 5.** UV–visible spectra for milling time $t = 0$ (reference), 1, 3, 5 and 7 h, at $\Omega =$ (**a**) 200 and (**b**) 400 rpm. The maximum absorbance obtained at 335 nm for pristine NPs was used as a reference to normalize all of the milled absorbance spectra. For non-normalized spectra, see supplementary figure S3.

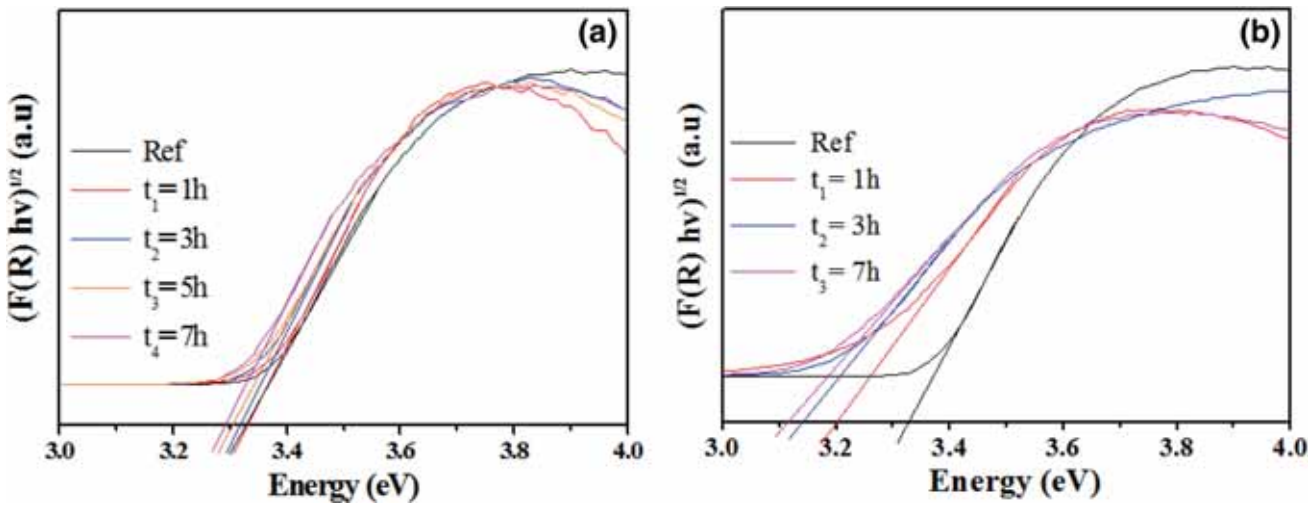


**Figure 6.** Variation of the band gap ($E_g$) according to Kubelka–Munk approach for milled $TiO_2$ NPs at $\Omega =$ (**a**) 200 and (**b**) 400 rpm, $E_g$ is estimated by the intercept of the Tauc plot of $(\alpha h\nu)^{1/2} \propto h\nu - E_g$ and the energy axis.

and d. Although the displayed results are rather scattered, they show clear trends in the evolution of these parameters: for both speeds, $E_g$ and $E_u$ have regular and opposite behaviours.

In summary, regardless of the applied speed, the milling of $TiO_2$ powder affects the light absorption properties of the powder. Furthermore, it is shown in figure 5 that from about 400 nm, the absorption curves are more spread out toward higher wavelength as the milling time increases. This is attributed to the formation of novel electronic states in the band gap at the $TiO_2$ nanoparticles surface [65], in agreement with the observed increase of Urbach energy together with the milling time. In $TiO_2$, $Ti^{4+}$ is surrounded by six oxygen ions forming the $TiO_6$ octahedral [66], high energy ball milling alters the arrangement of oxygen ions around $Ti^{4+}$ leading to either oxygen vacancies, while breaking the Ti–O bonds [67], or phase changes. This broadens the valence and conduction band edges, decreasing the gap energy, while increasing the Urbach energy [68]. As indicated by the XRD and HRTEM data comparison, it can be assumed that this process starts at the particle surfaces and propagate increasingly to the NP core as a function of energy.

### 4.2 *Photo-catalytic properties and ROS generation*

As already mentioned, the radical photo-generation is related to surface reactions. Therefore, the morphology of the NPs, the crystal phase as well as the surface states are the major parameters influencing the generation rate of the photo-mediated ROS. Semiconductors in aqueous suspension are known to generate reactive species upon illumination with

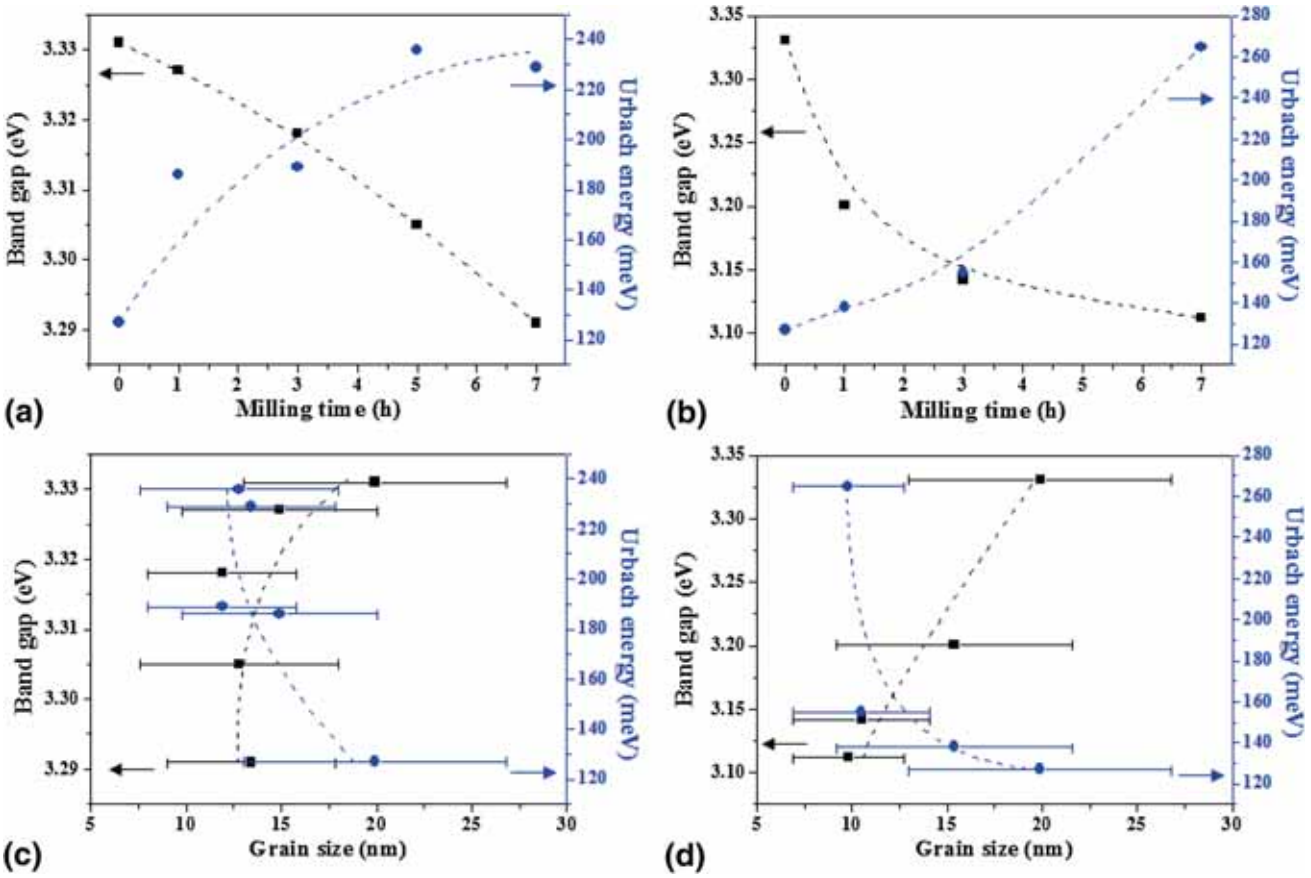


**Figure 7.** Variations of the band gap ($E_g$, black square) and Urbach energy ($E_u$, blue circle) with the milling time (upper panel) and resulting grain size (lower panel) for the two milling speeds: (**a** and **c**) 200 and (**b** and **d**) 400 rpm. Dashed lines are indicated as guide for the eyes.

photon energy equal or higher to the energy band gap. The photo-generated electrons and holes oxidize and reduce rapidly the molecular oxygen and water as shown in the following equations (5–7) [69], allowing the ROS generation such as $O_2^{\bullet-}$ and $HO^{\bullet}$, whose rate competes with the electron–hole recombination (equation (6)).

$$TiO_2 + h\nu \rightarrow e^- + h^+, \tag{4}$$

$$e^- + O_{2ads} \rightarrow O_2^{\bullet-}, \tag{5}$$

$$h^+ + H_2O_{ads} \rightarrow OH^{\bullet}, \tag{6}$$

$$e^- + h^+ \rightarrow h\nu(\text{recombination}). \tag{7}$$

Remarkably, other ROS can arise from the reactions described above (equations (5–7)), such as hydrogen peroxide and singlet oxygen [70,71]. Oxidation and reduction processes occur at the particle surface/solvent interface. The average lifetime of the photo-generated ROS being extremely short (from ns to μs at room temperature) when compared to the time of experiment, their evolution rate was estimated following two indirect methods: (i) the study of the degradation of the MO using UV–visible spectroscopy and (ii) spin-scavenging EPR technique using TEMPOL as paramagnetic probe. Figure 8 shows the decay of the normalized absorbance $(A(t)/A_0)$ recorded at $\lambda = 480$ nm for the reference sample and for all milled samples at the different speed and time conditions.

We notice that for both milling speeds, the normalized MO kinetic of degradation $(A(t)/A_0)$ slows down when the milling time increases. Interestingly, no photo-catalytic activity is detected (up to 210 min of illumination) for the highest energy milling ($\Omega = 400$ rpm) and for a milling time of 3 h and more (figure 8b).

To confirm this result, EPR spin-scavenging investigation was achieved [50,72]. The experiment was performed for the $TiO_2$ NPs, for the reference sample and for all the milling conditions. Figure 9 shows the decay of the EPR-normalized intensity $I(t)/I_0$ of TEMPOL as a function of the illumination time.

Similar to the MO degradation experiment, TEMPOL concentration decays as a function of UV-exposure time and the respective kinetics slow down when the milling time and/or speed is increased. The reduction of TEMPOL into EPR silent byproducts is mainly attributed here to $HO^{\bullet}$, $H^{\bullet}$ and/or $e^-$ [50]. At the highest milling speed and above 1 h of milling time, $I(t)/I_0$ curve remains flat despite 90 min of UV exposure in the presence of $TiO_2$ NPs. When compared to the

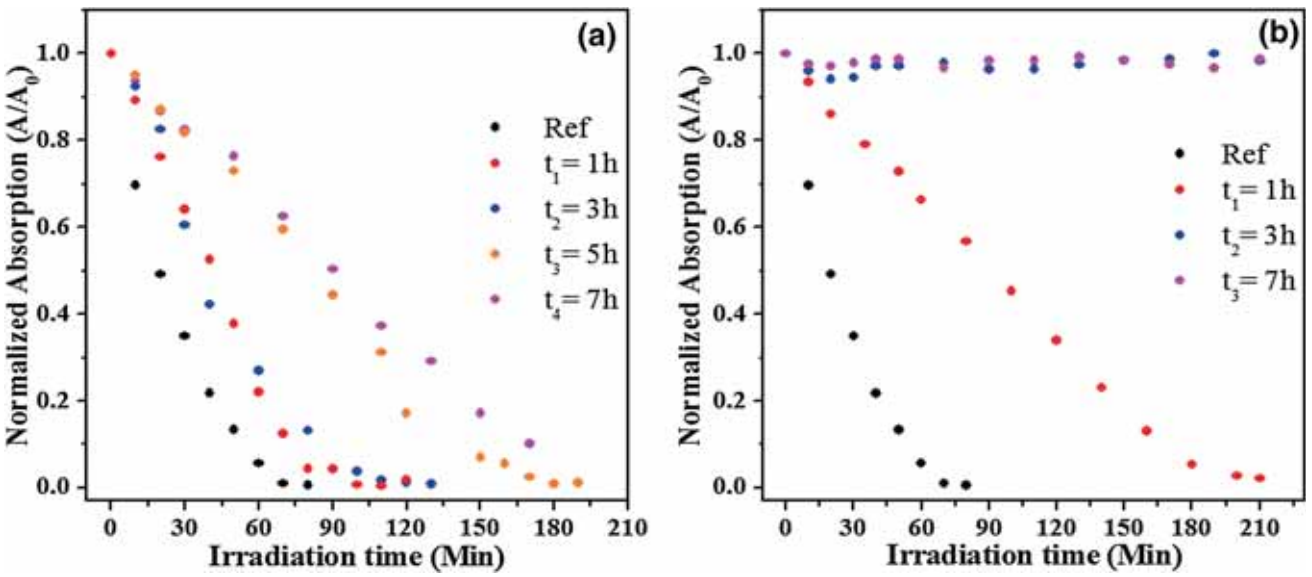


**Figure 8.** Photo-catalytic degradation, over time, of methylen orange in aqueous solution in the presence of $TiO_2$ NPs, for the milling times: $t = 0$ (reference), 1, 3, 5, 7 h at $\Omega =$ (**a**) 200 and (**b**) 400 rpm.

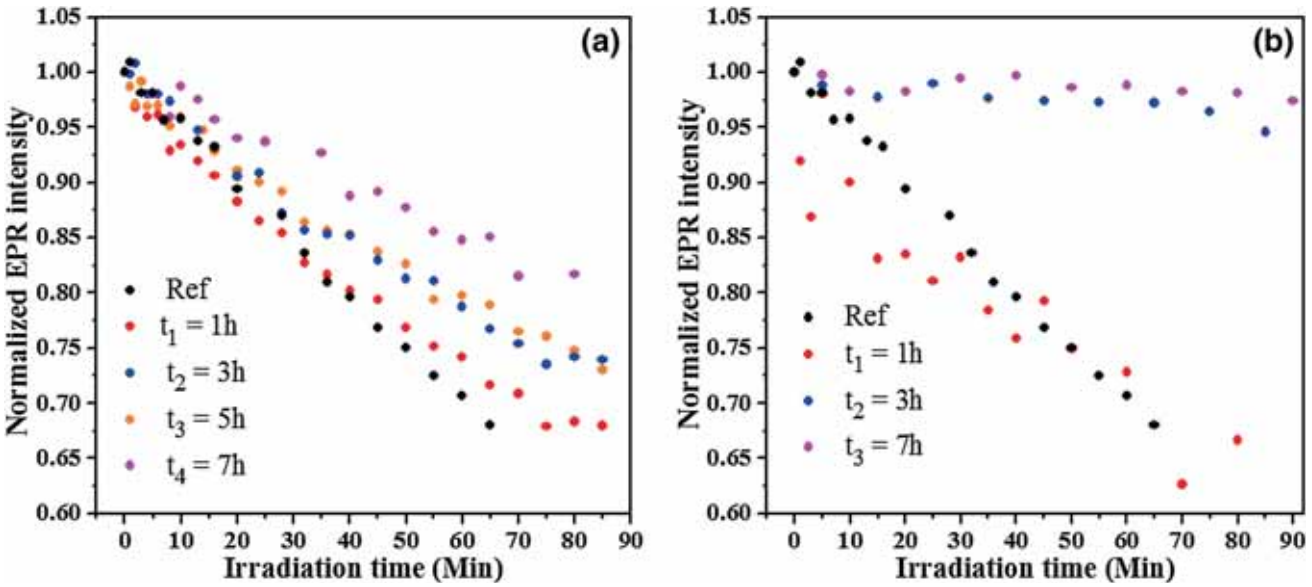


**Figure 9.** Evolution of TEMPOL-normalized EPR intensity, $I(t)/I_0$ as a function of time exposure to UV-light for the $TiO_2$ NPs aqueous suspension (0.1 g $l^{-1}$), $I_0$ being the intensity obtained prior to illumination. The data presented illustrate different milling speeds $\Omega =$ (**a**) 200 and (**b**) 400 rpm and milling times (1, 3, 5 and 7 h) as well as non-milled NPs (reference).

XRD investigation presented in this work, the degradation of the photo-catalytic properties coincides with the apparition of the amorphous phase of $TiO_2$ and surface states modification. Hence, neither the shift of the hydrodynamic diameter towards lower values (as shown in the DLS investigation, figure 4) nor the appearance of brookite phase (see XRD pattern of figure 1) influence neither the MO degradation nor the TEMPOL reduction.

In several studies, the amorphous phase is defined as a catalytically photo-inactive [47,73,74], due to a higher $e^-/h^+$ recombination rate [36]. However, even in the most altered structure investigated in this study (i.e., 7h milling at $\Omega = 400$ rpm), $TiO_2$ NPs do not appear fully inactive. Indeed, when supplementing the aqueous suspension of NPs with a sacrificial electron donor (such as EDTA), significant reduction of TEMPOL is observed (figure 10), yet delayed when compared to non-supplemented experiment (figure 9). The presence of such electron donor will neutralize the photogenerated holes, limiting $e^-/h^+$ recombination rate and therefore, increasing the lifetime of the photogenerated electrons available for TEMPOL reduction through direct pathway or indirect one ($H^\bullet$, $HO^\bullet$) [50]. Considering

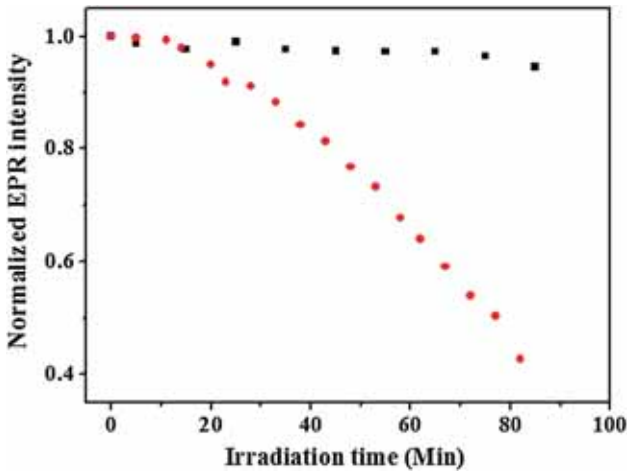


**Figure 10.** Evolution of normalized TEMPOL EPR intensity, $I(t)/I_0$ as a function of UV exposition time for the $TiO_2$ NPs (milled at 400 rpm for 7 h) in aqueous suspension (0.1 g $l^{-1}$), where $I_0$ is the EPR intensity obtained prior to illumination: with (filled circle) or without (filled square) sacrificial donor EDTA at 0.1 M, pH = 6.5.

the EPR kinetics, with or without EDTA, it appears that the MM does not hamper the overall generation of excitons, but rather drastically increases the recombination rate through newly generated electron traps. These new electronic levels arise from a modification of the electronic level distribution due to the presence of amorphous phase and thus, prevent the formation of reactive species and lead to the degradation of the photo-catalytic properties.

Finally, low temperature EPR ($T = 25$K) was also used to confirm how MM induces structural alteration of the NPs. On one hand, the EPR fingerprint of nano-$TiO_2$ in its anatase form [75–77] in the $g = 2$ region appears severely affected by MM (see supplementary figure S4) and is attributed to an increase in the amorphous phase and to induced disorder during milling. On the other hand, EPR spectra with larger sweep range (see supplementary figure S5) exhibit: (i) signals at $g = 4.31$ testimony of metallic high spin state attributed to Fe(III), and (ii) broad line ascribed to metallic contaminations [78]. Noteworthy, each of such tampering hallmarks is increasing with milling time and speed.

## 5. Conclusion

Structural consequences of planetary ball-milling process on $TiO_2$ NPs are manifold. Significant amorphization of $TiO_2$ related to the milling time and speed was demonstrated by TEM and XRD, while a weak phase transformation from anatase to brookite was observed. Such phase transformations play in favour of a degradation of the photo-catalytic activity. The diminution of grain size as a function of milling time and speed were characterized by TEM, while the hydrodynamic diameters obtained in aqueous suspension by DLS were determined. These later appear smaller at $\Omega = 200$ rpm and unchanged *ca.* at $\Omega = 400$ rpm. Such evolutions would suggest an increase in the photo-mediated generation of radicals for the lowest milling speed by increasing their respective available surfaces and an equivalent yield for the highest speed. However, the photogeneration activity assessed by MO degradation and EPR spin-scavenging are unquestionable and point toward a drastic degradation of the photo-catalytic activity concluding that no detectable activity for higher milling speed and milling time $\geq$3 h. The photo-catalytic activity seems to be affected much earlier than the occurrence of structural changes. However, the use of a sacrificial electron donor allows restoration of the activity, thus, pointing $e^-/h^+$ recombination as the limiting process. Finally, EPR at low temperature illustrated the disruption of anatase phase fingerprint as a function of both milling speed and time, and points towards metallic contamination.

## Acknowledgements

This study was supported by the CNRS (Centre National de la Recherche Scientifique) and Université de Strasbourg. We gratefully acknowledge Dr Marc Schmutz for his kind help in the TEM experiments. The authors thank the French Ministry of Research and the REseauNAtional de Rpeinter-Disciplinaire (RENARD, Fédération IR-RPE CNRS #3443).

## References

[1] Mozafari M R 2007 *Nanomaterials and nanosystems for biomedical applications* (Dordrecht, the Netherlands: Springer)
[2] Zhang L, Gu F, Chan J, Wang A, Langer R and Farokhzad O 2008 *Clin. Pharmacol.* **83** 761
[3] Mu L and Sprando R L 2010 *Pharm. Res.* **27** 1746
[4] Lee S, Cho I S, Lee J H, Kim D H, Kim D W, Kim J Y *et al* 2010 *Chem. Mater.* **22** 1958
[5] Zhong P and Que W X 2010 *Nano-Micro Lett.* **2** 1
[6] Jiang J, Oberdörster G and Biswas P 2009 *J. Nanoparticle Res.* **11** 77
[7] Yadav V 2013 *AEEE* **3** 771
[8] Pera-Titus M, García-Molina V, Baños M A, Giménez J and Esplugas S 2004 *Appl. Catal. B Environ.* **47** 219
[9] Singh R P, Singh P K and Singh R L 2014 *Toxicol. Int.* **21** 160
[10] Mazurkova N A, Spitsyna Y E, Shikina N V, Ismagilov Z R, Zagrebel'nyi S N and Ryabchikova E I 2010 *Nanotechnol. Russ.* **5** 417
[11] Franciscon E, Grossman M J, Paschoal J A R, Reyes F G R and Durrant L R 2012 *SpringerPlus* **1** 37
[12] Malato S, Fernández-Ibáñez P, Maldonado M I, Blanco J and Gernjak W 2009 *Catal. Today* **147** 1
[13] Tunç S, Gürkan T and Duman O 2012 *Chem. Eng. J.* **181** 431
[14] Du J, Lai X, Yang N, Zhai J, Kisailus D, Su F *et al* 2011 *ACS Nano* **5** 590
[15] Mo S D and Ching W Y 1995 *Phys. Rev. B* **51** 13023
[16] Djerdj I and Tonejc A M 2006 *J. Alloys Compd.* **413** 159

[17] Zhang J, Zhou P, Liu J and Yu J 2014 *Phys. Chem. Chem. Phys.* **16** 20382
[18] Kesselman J M, Shreve G A, Hoffmann M R and Lewis N S 1994 *J. Phys. Chem*. **98** 13385
[19] Xu M, Gao Y, Moreno E M, Kunst M, Muhler M, Wang Y *et al* 2011 *Phys. Rev. Lett*. **106** 138302
[20] Ozawa K, Emori M, Yamamoto S, Yukawa R, Yamamoto S, Hobara R *et al* 2014 *J. Phys. Chem. Lett.* **5** 1953
[21] Umezawa N, Shuxin O and Ye J 2011 *Phys. Rev. B* **83** 035202
[22] Yu J, Zhou P and Li Q 2013 *Phys. Chem. Chem. Phys*. **15** 12040
[23] Yu J C, Yu J, Ho W and Zhao J 2002 *J. Photochem. Photobiol. Chem*. **148** 331
[24] Chawengkijwanich C and Hayata Y 2008 *Int. J. Food Microbiol.* **123** 288
[25] Kim C, Park H, Cha S and Yoon J 2013 *Chemosphere* **93** 2011
[26] You D G, Deepagan V G, Um W, Jeon S, Son S, Chang H *et al* 2016 *Sci. Rep*. **6** 23200
[27] Sugimoto T, Zhou X and Muramatsu A 2003 *J. Colloid Interf. Sci.* **259** 43
[28] Zori M H 2010 *J. Inorg. Organomet. Polym. Mater*. **21** 81
[29] Shen X, Tian B and Zhang J 2013 *Catal. Today* **201** 151
[30] Kim S J, Park S D, Jeong Y H and Park S 1999 *J. Am. Ceram. Soc*. **82** 927
[31] McHale A E and Roth R S 1986 *J. Am. Ceram. Soc*. **69** 827
[32] Koch C C 2007 *Nanostructured materials: processing, properties, and applications* (Norwich, NY: William Andrew Pub) 2nd edn
[33] Shokrollahi H 2009 *Mater. Des*. **30** 3374
[34] Bensebaa Z, Bouzabata B, Otmani A, Djekoun A, Kihal A and Greneche J M 2009 *Phys. Procedia* **2** 649
[35] Prieto-Mahaney O O, Murakami N, Abe R and Ohtani B 2009 *Chem. Lett*. **38** 238
[36] Kominami H, Murakami S, Kato J, Kera Y and Ohtani B 2002 *J. Phys. Chem. B* **106** 10501
[37] Kočí K, Obalová L, Matějová L, Plachá D, Lacný Z, Jirkovský J *et al* 2009 *Appl. Catal. B Environ*. **89** 494
[38] Xu N, Shi Z, Fan Y, Dong J, Shi J and Hu M Z C 1999 *Ind. Eng. Chem. Res*. **38** 373
[39] Zhang X, Huo K, Wang H, Zhang W and Chu P K 2011 *J. Nanosci. Nanotechnol*. **11** 11200
[40] Yan J, Wu G, Guan N, Li L, Li Z and Cao X 2013 *Phys. Chem. Chem. Phys*. **15** 10978
[41] Vargeese A A and Muralidharan K 2011 *J. Hazard. Mater.* **192** 1314
[42] Liu B, Zhao X, Yu J, Fujishima A and Nakata K 2016 *Phys. Chem. Chem. Phys*. **18** 31914
[43] de Carvalho J F, de Medeiros S N, Morales M A, Dantas A L and Carriço A S 2013 *Appl. Surf. Sci*. **275** 84
[44] Rezaee M and Mousavi Khoie S M 2010 *J. Alloys Compd*. **507** 484
[45] Bégin-Colin S, Gadalla A, Le Caër G, Humbert O, Thomas F, Barres O *et al* 2009 *J. Phys. Chem. C* **113** 16589
[46] Saitow K and Wakamiya T 2013 *Appl. Phys. Lett*. **103** 031916
[47] Ohtani B, Ogawa Y and Nishimoto S 1997 *J. Phys. Chem. B* **101** 3746
[48] Aggelopoulos C A, Dimitropoulos M, Govatsi A, Sygellou L, Tsakiroglou C D and Yannopoulos S N 2017 *Appl. Catal. B: Environ*. **205** 292
[49] Yamato M, Kawano K, Yamanaka Y, Saiga M and Yamada K 2016 *Redox Biol*. **8** 316
[50] Martel D, Guerra A, Turek P, Weiss J and Vileno B 2016 *J. Colloid Interf. Sci*. **467** 300
[51] Vileno B, Turek P, Weiss J and Martel D 2013 *ChemPlusChem* **78** 1330
[52] Sugapriya S, Sriram R and Lakshmi S 2013 *Opt. Int. J. Light Electron Opt*. **124** 4971
[53] Langford J I and Wilson A J C 1978 *J. Appl. Crystallogr.* **11** 102
[54] Kim S H, Lee Y J, Lee B H, Lee K H, Narasimhan K and Kim Y D 2006 *J. Alloys Compd*. **424** 204
[55] Suryanarayana C 2001*Prog. Mater. Sci*. **46** 1
[56] Reyes-Coronado D, Rodríguez-Gattorno G, Espinosa-Pesqueira M E, Cab C, de Coss R and Oskam G 2008 *Nanotechnology* **19** 145605
[57] Zhao H, Liu L, Andino J M and Li Y 2013 *J. Mater. Chem. A* **1** 8209
[58] Jassby D, Farner Budarz J and Wiesner M 2012 *Environ. Sci. Technol.* **46** 6934
[59] Melcher J, Barth N, Schilde C, Kwade A and Bahnemann D 2017 *J. Mater. Sci*. **52** 1047
[60] Choudhury B, Dey M and Choudhury A 2013 *Int. Nano Lett*. **3** 25
[61] Burgeth G and Kisch H 2002 *Coord. Chem. Rev*. **230** 41
[62] Simmons E L 1975 *Appl. Opt*. **14** 1380
[63] Kortüm G 2012 *Reflectance spectroscopy: principles, methods, applications* (Berlin: Springer)
[64] Grundmann M 2010 *The physics of semiconductors—an introduction including* (Heidelberg, Berlin: Springer)
[65] Indris S, Amade R, Heitjans P, Finger M, Haeger A, Hesse D *et al* 2005 *J. Phys. Chem. B* **109** 23274
[66] Paul S and Choudhury A 2014 *Appl. Nanosci*. **4** 839
[67] Hidalgo M C, Colón G and Navío J A 2002 *J. Photochem. Photobiol. Chem*. **148** 341
[68] Zhang Y, Chen J and Li X 2010 *Catal. Lett*. **139** 129
[69] Vileno B, Lekka M, Sienkiewicz A, Jeney S, Stoessel G and Lekki J 2007 *Environ. Sci. Technol.* **41** 5149
[70] Moon G, Kim W, Bokare A D, Sung N and Choi W 2014 *Energy Environ. Sci*. **7** 4023
[71] Chen W and Zhang J 2006 *J. Nanosci. Nanotechnol*. **6** 1159
[72] Vileno B, Marcoux P R, Lekka M, Sienkiewicz A, Fehér T and Forró L 2006 *Adv. Funct. Mater*. **16** 120
[73] Ide Y, Inami N, Hattori H, Saito K, Sohmiya M, Tsunoji N *et al* 2016 *Angew. Chem. Int. Ed. Engl*. **55** 3600
[74] Gao L and Zhang Q 2001 *Scr. Mater.* **44** 1195
[75] Fenoglio I, Greco G, Livraghi S and Fubini B 2009 *Chem. Weinh. Bergstr. Ger.* **15** 4614
[76] Kumar C P, Gopal N O, Wang T C, Wong M S and Ke S C 2006 *J. Phys. Chem. B* **110** 5223
[77] Attwood A L, Murphy D M, Edwards J L, Egerton T A and Harrison R W 2003 *Res. Chem. Intermed*. **29** 449
[78] Graetzel M and Howe R F 1990 *J. Phys. Chem*. **94** 2566